Journal of Energy Storage 182 (2026) 124894

Contents lists available at ScienceDirect

Journal of Energy Storage

journal homepage: www.elsevier.com/locate/est

Research papers

Metal organic framework derived cobalt phosphide nitrogen-doped carbon coated by cobalt-manganese oxide nanoflakes and two-dimensional MXene based electrodes for energy-dense quasi-solid-state supercapacitors

Arti A. Jadhav [a], Amar M. Patil [b,c,**], Seongyeon Hwang [d], Jongwoo Hong [b], Ganesh D. Jadhav [a], Suprimkumar D. Dhas [e], Tayebeh Ameri [c], Kyeounghak Kim [d,**], Seong Chan Jun [b,**], Umakant M. Patil [a,*]

[a] Centre for Interdisciplinary Research, D. Y. Patil Education Society, Kasaba Bawada, Kolhapur, 416006, India
[b] Nano-Electro-Mechanical Device Laboratory School of Mechanical Engineering, Yonsei University, Seoul, 120-749, Republic of Korea
[c] Department of Materials Science, Faculty of Engineering, Christian-Albrechts-Universität zu Kiel, Kaiserstraße, 2, Kiel, 24143, Germany
[d] Department of Chemical Engineering, Hanyang University, Seoul, 04763, Republic of Korea
[e] UAEU Science & Innovation Park, United Arab Emirates University, Al Ain, United Arab Emirates

ARTICLE INFO

Keywords:
Metal-organic frameworks (MOFs)
Core-shell materials
Cobalt phosphide (CoP) and cobalt manganese oxide
MWCNT/MXene composite electrode
Quasi-solid-state supercapacitor

ABSTRACT

Transition metal phosphides derived from metal-organic framework (MOF) offers high electronic conductivity and porous electrode architectures; however, their relatively poor structural stability significantly affects the overall performance of supercapacitors. To overcome this limitation, MOF-derived cobalt phosphide nanoparticles are directly deposited on nitrogen (N)-doped carbon micro-petals (Co_xP_yNC) and further coated with cobalt-manganese oxide ($Co_2MnO_{4.5}$) nanoflakes using successive ionic layer adsorption and reaction (SILAR) method to make core-shell ($Co_2MnO_{4.5}$@Co_xP_yNC). The novelty lies in constructing a core-shell electrode, where the pyrolysis-derived porous and conductive N-doped carbon network enhances charge transport and provides abundant electroactive sites for superior electrochemical performance, as further supported by density functional theory calculations. The adsorption energy of $Co_2MnO_{4.5}$@Co_xP_yNC of −5.57 eV is considerably more negative than that of bare CoP of −3.76 eV, indicating stronger electrolyte-ion adsorption and enhanced surface-electrolyte interaction. The electrode demonstrates an excellent 725.8 F g^{-1} specific capacitance at 0.5 mA cm^{-2}. A quasi-solid-state device (QSSD) is fabricated with a multiwalled carbon nanotube (MWCNT)/$Ti_3C_2T_x$-MXene electrode using gel electrolyte. The assembled QSSD delivered a maximum 183.9 F g^{-1} specific capacitance at 0.25 A g^{-1}, energy density of 50.06 Wh kg^{-1} and excellent 96.5% capacitance retention for 10,000 cycles.

1. Introduction

The development of environmentally friendly and efficient renewable technologies for rapid energy storage and conversion has become crucial in response to the energy crisis of the past decades [1–3]. Recently, the supercapacitor (SC) has gained attention in contrast to other energy storage technologies, due to a distinct combination of high-power, long-term stability and fast charging [4,5]. Nevertheless, the low energy of most SC remains a major challenge which limits their widespread use. Hybrid energy storage systems that integrate capacitive-type electrodes with high-power density and battery-type electrodes capable of delivering high capacity provide a promising solution to the limitations of carbon-based commercial capacitors [6]. Tuning the surface structure and charge-storage properties of electrodes by combining two or more materials through different strategies, along with the development of high energy SC devices, remains a significant challenge [7].

Metal-organic frameworks (MOFs) are outstanding precursors and

* Correspondence to: U. M. Patil, Centre for Interdisciplinary Research, D. Y. Patil Education Society, Kasaba Bawada, Kolhapur, 416006, India.
** Corresponding authors.
E-mail addresses: amarpatil212@gmail.com (A.M. Patil), chemekim@hanyang.ac.kr (K. Kim), scj@yonsei.ac.kr (S.C. Jun), umpatil.cir@dypgroup.edu.in (U.M. Patil).

https://doi.org/10.1016/j.est.2026.124894
Received 3 July 2026; Received in revised form 5 September 2026; Accepted 22 September 2026
Available online 9 October 2026
2352-152X/© 2026 Elsevier Ltd. All rights are reserved, including those for text and data mining, AI training, and similar technologies.

templates, offering properties such as tunable pore size, high porosity, and structural stability for creating a nanostructure [8,9]. Specifically, Zeolitic Imidazolate Framework-67 (ZIF-67) displays a cage-like structure that facilitates the formation of core-shell, enhancing mass transport and minimizing ion diffusion pathways and cavities, which can encapsulate electroactive sites [10,11]. Several MOF-derived advanced electrodes have been explored to synthesize transition metal phosphides (TMPs) and their composites with materials such as phosphates (TMPOs), sulfides (TMSs), and oxides (TMOs), containing various architectures for electrode material of energy storage systems [8,12]. TMPs have low cost and higher electrical conductivity compared to TMOs, excellent reversible redox reactions, and high theoretical capacity [13]. Cobalt (Co) and manganese (Mn) based TMOs and their composites have been extensively investigated as SC electrodes owing to their natural abundance, multiple valence states (Co^{2+}, Co^{3+}, Mn^{3+}, Mn^{4+}), high specific capacitance (C_s), structural versatility, and excellent electrochemical stability [14–17]. Two primary challenges of TMOs-based materials are low electronic conductivity and large volume change during redox reactions, which severely restrict their practical applications [6]. Core-shell TMOs-based designs provide a promising strategy to address these limitations [18–20]. TMOs-based core-shell structures have garnered promising among multi-component nanomaterials due to their exceptional properties, including versatility, low cost, tunability, and stability. Chen et al. synthesized, Ni-Co-P/PO_x with phosphidation method and reported 647C g^{-1} capacity at 1 A g^{-1} [21]. Chen et al. prepared CuO@MnO_2 core-shell materials and reported C_s of 252.6 F g^{-1} at 0.1 A g^{-1} [22]. Bao et al. produced the core-shell nanocable structured Zn_2SnO_4/MnO_2 and reported C_s of 642.4 F g^{-1} [23]. Core-shell nanoparticles (NPs) are typically defined as composite nanomaterials comprising an inner core and an outer shell. A thin shell layer is advantageous, as charge storage predominantly occurs at the surface. Therefore, integrating TMPs and TMOs in a core-shell structure represents a promising strategy with combining cobalt phosphide and cobalt manganese oxide.

In this study, core-shell electrode materials were synthesized using a MOF-derived Co_xP_yNC core on carbon cloth (CC), deposited through binder-free co-precipitation and phosphidation processes, and a $Co_2MnO_{4.5}$ shell, which was subsequently deposited using an successive ionic layer adsorption and reactions (SILAR) method. The $Co_2MnO_{4.5}$ nanoflake shell acts as a protective layer over the Co_xP_yNC core NPs, providing additional electroactive sites for electrochemical reactions and preventing the rapid degradation of the core material during electrochemical cycling. The Co_xP_yNC core material provides high electrical conductivity, while the $Co_2MnO_{4.5}$ shell contributes abundant electroactive surface sites, facilitating enhanced charge transfer throughout the electrode. The adsorption energy of the core-shell material (−5.57 eV) is higher than that of the bare core material (−3.76 eV), which supports the improved storage capacity of electrode. The quasi-solid-state device (QSSD) displayed an excellent C_s of 183.9 F g^{-1} and 50.06 Wh kg^{-1} energy, along with C_s retention of 96.5% after 10,000 cycles.

2. Result and discussion

2.1. $Co_2MnO_{4.5}$@Co_xP_yNC/CC MOF-derived positive electrodes

MOF-derived Co_xP_yNC TMPs were directly deposited on CC conductive substrates through sequential co-precipitation, pyrolysis, and phosphidation processes [19,24]. Furthermore, the $Co_2MnO_{4.5}$ TMOs were deposited onto Co_xP_yNC/CC using the SILAR method, forming a $Co_2MnO_{4.5}$@Co_xP_yNC/CC core-shell positive electrode

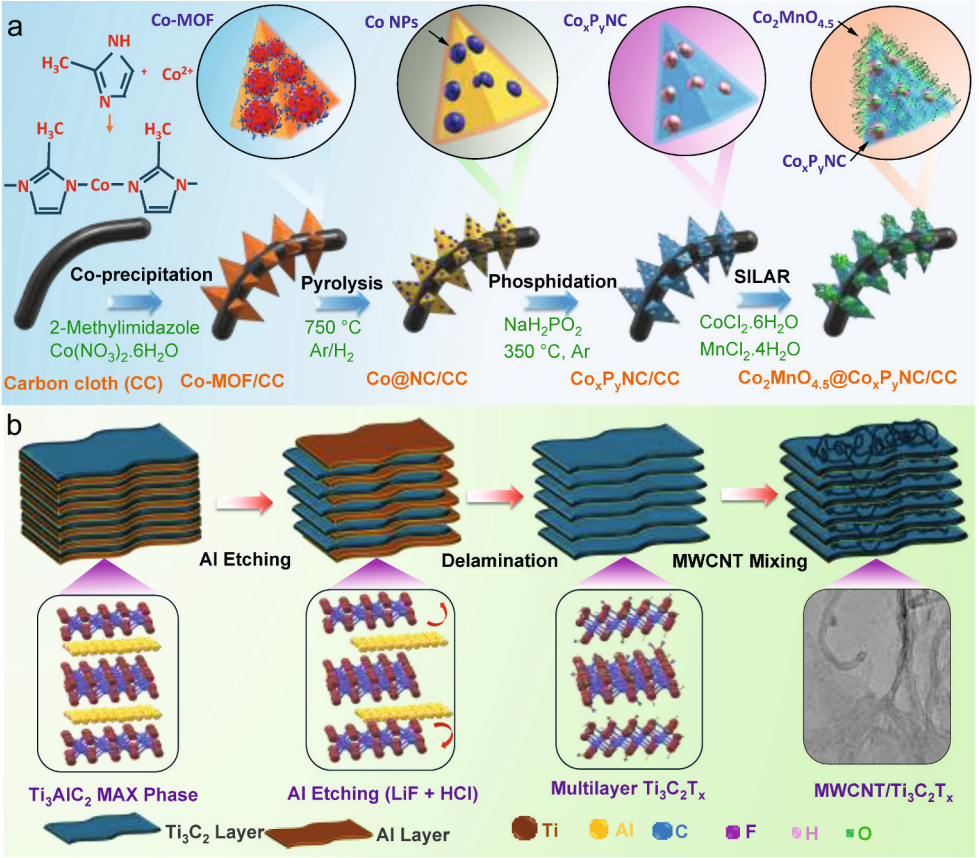

Fig. 1. (a) Schematic of development of $Co_2MnO_{4.5}$@Co_xP_yNC/CC core-shell using phosphidation and SILAR methods, and (b) MWCNT/MXene development using etching, delamination and exfoliation.

(Fig. 1a). The electrodes with different SILAR cycles of 10, 20, 30 and 40 were abbreviated as $Co_2MnO_{4.5}$@Co_xP_yNC/CC-10-40, respectively. $Ti_3C_2T_X$-MXene was produced from Ti_3AlC_2-MAX phase by Al etching [25–28]. The delaminated and exfoliated two-dimensional (2D) MXene sheets were then mixed with multiwalled carbon nanotube (MWCNT) and subsequently drop-casted onto CC to fabricate the MWCNT/MXene/CC negative electrode (Fig. 1b). Detailed experimental procedures are provided in the experimental section in Supporting Information.

Surface structure analysis and the morphological evolution of the core-shell electrode surface during SILAR cycle variation from 10 to 40 cycles have been confirmed by scanning electron microscopy (SEM) images. The SEM images verify that the shell material is uniformly coated onto the core surface. The development of $Co_2MnO_{4.5}$ shell nanoflakes on the Co_xP_yNC micro-petals-like core was depicted in Fig. 2a-d. These nanoflakes are comparatively thin and randomly aligned across the micro-petals for the $Co_2MnO_{4.5}$@Co_xP_yNC/CC-10 and $Co_2MnO_{4.5}$@Co_xP_yNC/CC-20 electrodes. Even with the thick coating, there are noticeable defects with surface roughness, representing that the individual flakes have not yet fully consolidated. In Fig. 2e and f, nanoflakes have developed sharper edges and grown densely on the core material. As the number of cycles increased, the vertical growth much enhanced, and full-sized nanoflakes were clearly visible on the surface. A more robust "rose-petal" or "honeycomb-like" shape has been seen in these samples. For the $Co_2MnO_{4.5}$@Co_xP_yNC/CC-30 electrode, this structural evolution associated with enough electroactive sites offered at 30 SILAR cycles, providing greater accessible internal surface area for electrolyte ions. Upon closer inspection, it is seen that the thickness and density of the deposited material have risen dramatically with each subsequent SILAR cycles. Individual flakes are more densely packed, and additional nucleation appears to have happened on the borders of existing nanoflakes structures, which is useful for applications that need a large effective surface area. For the $Co_2MnO_{4.5}$@Co_xP_yNC/CC-40 electrode, material deposition increases with the number of cycles, resulting in loosely packed nanoflakes that peel off from the core material (Fig. 2g and h). The comparative SEM pictures of Co_xP_yNC are depicted in Fig. S1a-c.

Transmission electron microscopy (TEM) images of $Co_2MnO_{4.5}$@-Co_xP_yNC/CC-30 core-shell material revealed a complex, heterogeneous structure of micro-petals, with the dark, dense spots represented by the red dashed circles being Co_xP_y NPs distributed across the N doped carbon matrix (Fig. 2i-k). The regions indicated by the yellow dashed circles are thin layers of the $Co_2MnO_{4.5}$ shell material. The high-resolution TEM

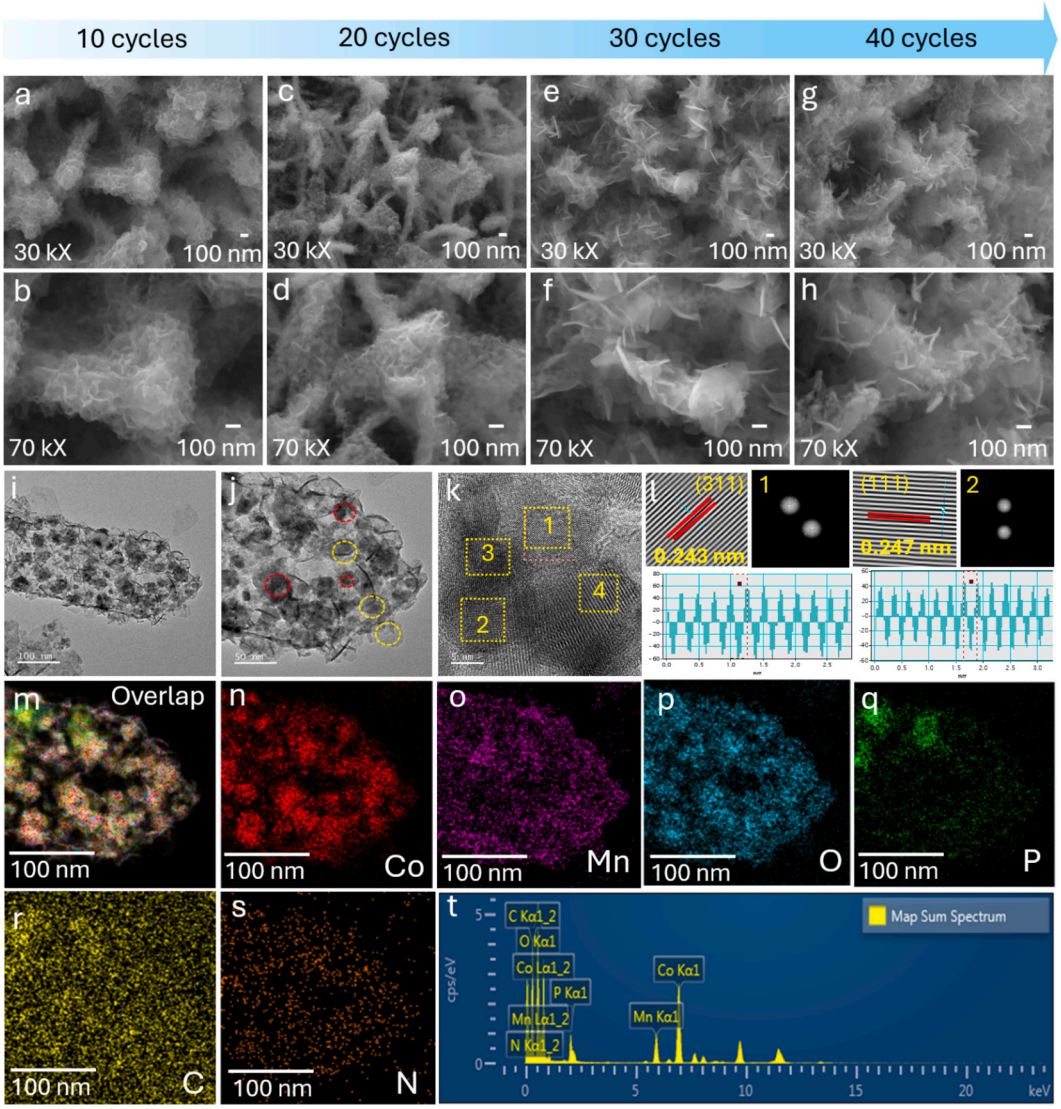

Fig. 2. (a-h) SEM images of $Co_2MnO_{4.5}$@Co_xP_yNC/CC-10, $Co_2MnO_{4.5}$@Co_xP_yNC/CC-20, $Co_2MnO_{4.5}$@Co_xP_yNC/CC-30, and $Co_2MnO_{4.5}$@Co_xP_yNC/CC-40 electrodes at 30 kX and 70 kX, (i-k) TEM images of the $Co_2MnO_{4.5}$@Co_xP_yNC/CC-30, (l) Line profile fitting and SAED patterns at positions 1 and 2 of figure k, (m-s) Elemental mapping of the $Co_2MnO_{4.5}$@Co_xP_yNC/CC-30 for overlap, Co, Mn, O, P, C and N, and (t) Corresponding EDS spectrum.

(HRTEM) image Fig. 2l and Fig. S2a-c revealed interplanar spacings of 0.247 nm and 0.279 nm with (111) and (002) planes of Co_xP_y, and 0.243 nm and 0.467 nm, which are indexed to (311) and (111) planes of $Co_2MnO_{4.5}$, respectively [15,29]. Also, the polycrystalline nature and appropriate hkl planes with several diffraction rings are identified in the selected area electron diffraction (SAED) (Fig. S2d). The diffraction rings corresponding to the (011), (111), and (301) planes of CoP and the (111), (400), and (440) planes of $Co_2MnO_{4.5}$ are also visible in the SAED picture [30]. The HRTEM and SAED results indicate that the $Co_2MnO_{4.5}$@Co_xP_yNC core-shell structure was successfully developed, and these findings are supported by X-ray diffraction (XRD) results. Furthermore, elemental mapping analysis with energy dispersive X-ray spectroscopy (EDS) verified the effective development of $Co_2MnO_{4.5}$ shell on Co_xP_yNC core structure. Figs. 2m-t depict the TEM-EDS analysis of the $Co_2MnO_{4.5}$@Co_xP_yNC-30 electrode. The surface elemental mapping approves the existence of Co, Mn, O, P, N, as well as C elements, which are uniformly distributed.

The XRD analysis verifies the crystal structures of electrode materials (Fig. 3a). The all $Co_2MnO_{4.5}$@Co_xP_yNC/CC-10 to 40 core-shell electrodes display a similar XRD patterns with changing the intensities of the peaks. The strong peaks observed at 18.5, 59.4, and 65.3° with plane (111), (511), (440) well matched to JCPDS card No-0320297 which is corresponding to $Co_2MnO_{4.5}$ material [31,32]. Furthermore, the peaks observed at 31.6 and 48.1° with plane (011, (211) respectively are corresponding to CoP (JCPDS card No-0290497) [33]. The intensity of the peak at 36° is observed to be increasing with repeating SILAR cycles from 10 to 40 indicating the increment in the growth of $Co_2MnO_{4.5}$ material.

Fig. 3b and Fig. S3a shows the Raman spectrum of $Co_2MnO_{4.5}$@-Co_xP_yNC/CC-30 electrode, which displays several well-defined vibrational bands that originate from metal-oxygen (M-O) interactions and lattice dynamics within the mixed Co—Mn oxide framework. The band observed at ~186 cm^{-1} in the low-frequency range is attributed to lattice vibrational modes associated to the collective motion of Co and Mn

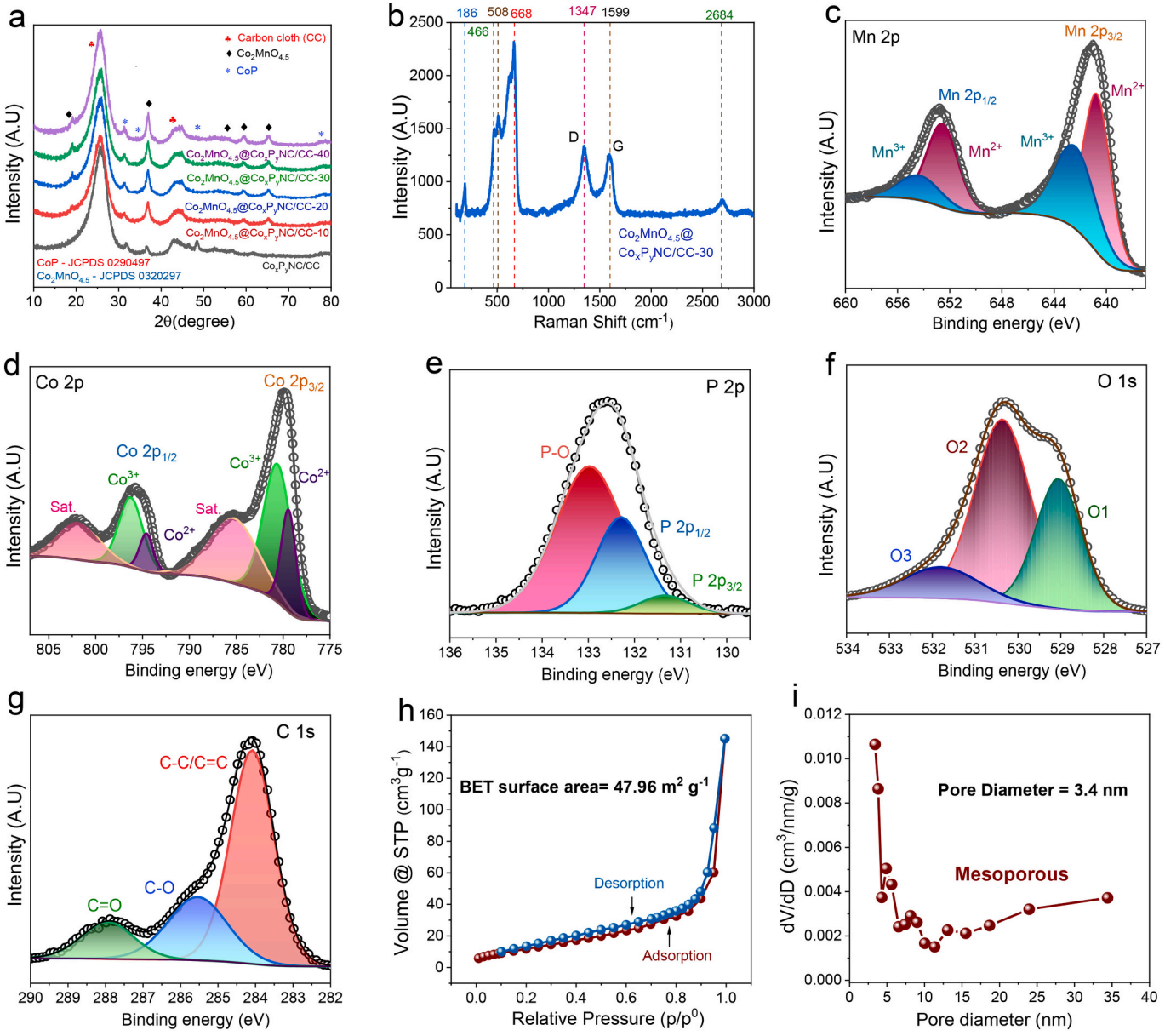

Fig. 3. (a) XRD patterns of $Co_2MnO_{4.5}$@Co_xP_yNC/CC-10 to 40 electrodes, (b) Raman spectrum of $Co_2MnO_{4.5}$@Co_xP_yNC/CC-30 electrode, deconvoluted spectra of (c-g) Mn 2p, Co 2p, P 2p, O 1 s, and C 1 s, respectively, and (h and i) N_2 adsorption and desorption isotherms and BJH pore size plots of the $Co_2MnO_{4.5}$@Co_xP_yNC/CC-30 material.

cations, which shows the framework of M-O oxide is long-range ordering [32]. The peak positioned at ~466 cm^{-1} links to symmetric bending vibrations of O-Co/Mn-O indicating strong coupling between oxygen atoms and the surrounding Co or Mn metals [32]. The strong peak positioned at ~668 cm^{-1} resulted as of symmetric stretching of Co—O bonds [34], indicating the building of a strong Co—Mn oxide lattice, whereas the band at ~508 cm^{-1} is ascribed to asymmetric stretching vibrations of Mn—O bonds [32,35]. The band at ~1347 cm^{-1} in the high-frequency range is the defect peak of carbon (marked as D), which is corresponding to defects in structure, and heteroatom doping of N or P in the carbon framework [33]. The existence of graphitic domains is indicated by the G band (marked as G), which is at ~1599 cm^{-1} and comes from in-plane vibrations of sp^2-bonded carbon atoms [33]. The I_D/I_G intensity ratio of the two peaks is 1.21, indicating the $Co_2MnO_{4.5}$@Co_xP_yNC/CC core-shell material is defect-rich carbon structure [36]. The 2D band corresponds to disordered or few-layer graphitic carbon with weak band is observed at ~2684 cm^{-1}. The Raman analysis confirms the successful integration of Co-Mn-oxide species with heteroatom-doped carbon, which is favorable to promote charge transfer within electrode material.

X-ray photoelectron spectroscopy (XPS) measurement determines the chemical composition and valence states of $Co_2MnO_{4.5}$@Co_xP_yNC/CC. The appearance of Mn, Co, C, O, P, as well as N elements in the XPS survey spectra confirms the formation of $Co_2MnO_{4.5}$@Co_xP_yNC/CC-30 (Fig. S3b). In the deconvoluted Mn 2p spectra, the two primary peaks of Mn $2p_{3/2}$ along with Mn $2p_{1/2}$ splits into four independent peaks, as shown in Fig. 3c. Two separate peaks positioned at 640.76 eV and 652.68 eV show the presence of Mn^{2+} [32]. The Mn^{3+} corresponding peaks are observed at 654.54 eV and 642.63 eV [37]. The Co 2p spectra, shown in Fig. 3d, depict two peaks at 779.83 eV and 795.50 eV, corresponding to Co $2p_{3/2}$ and Co $2p_{1/2}$, separated by 15.67 eV. The Co $2p_{3/2}$ and Co $2p_{1/2}$ are comparable to the binding energies of the Co^{2+} besides Co^{3+} peaks, which are positioned at 780.58 eV and 797.65 eV, respectively [32,38]. The Co^{2+} diffraction peaks at 779.81 eV and 794.61 eV, while Co^{3+} diffraction peaks at 780.75 eV and 796.25 eV, respectively. The satellite peaks are observed for the Co $2p_{3/2}$ and Co $2p_{1/2}$ at 785.24 eV and 802.10 eV, respectively. In Fig. 3e, the three peaks at 133.06, 132.26, and 131.17 eV of the P 2p spectra are representing the P—O bond, P $2p_{1/2}$, as well as P $2p_{3/2}$ of M-P, respectively [39]. Fig. 3f shows O 1 s high-resolution spectrum fitted with three peaks denoted by the letters O1, O2, along with O3. The O1 component at 529.05 eV corresponds to common metal-oxygen bonds [40]. A higher defect sites with poor oxygen coordination are associated with the well-resolved O2 component at around 530.38 eV, moreover, the quantity of physio and chemisorbed water close to the surface is attributed to the O3 component at 531.83 eV [37]. The C1s peaks at 287.86, 285.53 and 284.08 eV in the samples are attributed to the C═O, C—O as well as C-C/C=C respectively (Fig. 3g). The originated C 1 s peaks also might be corresponding to the CC [25].

N_2-adsorption/desorption isotherms determine the surface area of $Co_2MnO_{4.5}$@Co_xP_yNC electrode material (Fig. 3h). The mesoporous structure with type IV isotherms together with H_3 type hysteresis is observed. The surface area of the $Co_2MnO_{4.5}$@Co_xP_yNC material is observed to be 47.96 $m^2\ g^{-1}$ which is suitable for the higher charge storage capacity. The observed surface area resulted from uniform growth of $Co_2MnO_{4.5}$ nanoflakes on the Co_xP_yNC micro-petals, increasing their porosity and providing additional material surfaces for electrochemical processes. To understand the distribution of pore diameters in the materials, Barrett-Joyner-Halenda (BJH) analysis was conducted Fig. 3i. The higher percentage of the pores available at 3.4 nm indicates that mesoporous architectures of materials and its size is large enough for diffusion of small molecules and ions for good mass transport of electrolyte. Additionally, the effective synthesis of $Co_2MnO_{4.5}$@Co_xP_yNC/CC sample is verified by Fourier transform infrared spectroscopy (FTIR) studies in Fig. S4. The broad absorption band observed at 3434 cm^{-1} for intermolecular hydrogen-bonded hydroxyl groups which indicates that the sample surface has -OH groups [41]. The bands at 2911 cm^{-1} links to the sp^3 C—H stretching, 1629 cm^{-1} besides 668 cm^{-1} links to H-O-H bending and Mn-O/Co-O stretching modes of the $Co_2MnO_{4.5}$ [41]. The 1057 cm^{-1} and 668 cm^{-1} peaks are corresponding to P—O besides Co—P [33].

2.2. *Electrochemical measurements of $Co_2MnO_{4.5}$@Co_xP_yNC/CC positive electrodes*

The cyclic voltammetry (CV) test of the electrodes was measured within −0.2 to 0.5 V *vs* SCE. The relative CV curves of the $Co_2MnO_{4.5}$@Co_xP_yNC/CC and Co_xP_yNC demonstrated significant increment in integral area inside CV curves of core-shell electrodes compared with Co_xP_yNC (Fig. 4a). The CV curves displayed a nearly symmetric charge discharge profile with anodic and cathodic peaks, indicating the charge stored by faradaic reactions [26,42]. The reversible redox transitions of Co and Mn species (Co^{2+}/Co^{3+} and Mn^{2+}/Mn^{3+}) correspond to significant oxidation peaks in the anodic curve within 0.05–0.30 V *vs* SCE, indicating surface-controlled charge storage. Notably, the $Co_2MnO_{4.5}$@Co_xP_yNC/CC core-shell electrode exhibits considerably better anodic current response at ~0.4–0.5 V *vs* SCE, reflecting enhanced electrical conductivity and faster charge-transfer kinetics compared to the pristine Co_xP_yNC [29]. When $Co_2MnO_{4.5}$ is incorporated into Co_xP_yNC, the cathodic current increases during the reverse scan, suggesting that the redox processes are more reversible and that surface intermediates produced during oxidation are effectively reduced. The CV curves of the optimized $Co_2MnO_{4.5}$@Co_xP_yNC/CC-30 electrode with superior storage performance and high-rate capabilities are depicted in Fig. 4b [43]. To investigate further in depth the reaction kinetics, the log (i) *vs* log (s) plots were fitted to estimate the b-value and confirm the type of charge storage (Fig. 4c) [44]. The $Co_2MnO_{4.5}$@Co_xP_yNC/CC-30 electrode exhibited a 0.93 b-value therefore, indicating a capacitance-controlled process (Q_s). The total charge (Q_t) distribution from with addition of charge from Q_s and charge from diffusion-controlled reactions (Q_d) are calculated within 5–100 mV s^{-1} and depicted in Fig. 4d-f. To calculate the Q_b, the following formula is used for quantitative analysis of the Q_s and Q_d [44–46].

$$i_p\ (V) = k_1\nu + k_2\nu^{1/2} \quad (1)$$

where $k_1\nu$ represents capacitance and $k_2\nu^{1/2}$ represent diffusion contributed peak current, respectively. The $Co_2MnO_{4.5}$@Co_xP_yNC/CC-30 electrode exhibits a Q_s, gradual rise from 23.28% to 76.71% as the scan rates are enlarged from 5 to 100 mV s^{-1} (Fig. 4e). This result shows that the Q_s contributes more to charge storage on $Co_2MnO_{4.5}$@Co_xP_yNC/CC the electrode, validating the results getting from b value.

The comparative galvanostatic charge-discharge (GCD) curves of the $Co_2MnO_{4.5}$@Co_xP_yNC/CC-10-40 and Co_xP_yNC/CC electrodes are depicted in Fig. 4g, demonstrating the non-linear curves which confirms faradaic processes. GCD curves of the $Co_2MnO_{4.5}$@Co_xP_yNC/CC-30 optimized electrode within −0.2-0.4 V/SCE at 0.5–4 mA cm^{-2} is depicted in Fig. 4h. The charge stored on the electrodes due to the faradic reactions with reversible Co^{2+}/Co^{3+} and Mn^{2+}/Mn^{3+} transitions at interfaces [46–48]. Furthermore, the Co_xP_yNC provides highly conductive paths that speed up electron movement and encourage effective use of redox-active sites. The extended discharge time observed for $Co_2MnO_{4.5}$@Co_xP_yNC/CC-30 core-shell electrode, compared with pristine Co_xP_yNC components, indicates enhanced charge storage capability arising from the synergistic interaction between the Co_xP_yNC and $Co_2MnO_{4.5}$. Additionally, the very low potential drop during the GCD indicates minimal internal resistance, which highlight the enhanced electrical conductivity and rapid response kinetics. The optimized electrode $Co_2MnO_{4.5}$@Co_xP_yNC/CC-30 delivered a C_s of 725.8, 661.47, 623.65, 572.58, and 550.63 F g^{-1} at 0.5–4 mA cm^{-2}, respectively (Fig. 4i). The electrochemical impedance spectroscopy was employed to evaluate the interfacial resistances of the core-shell

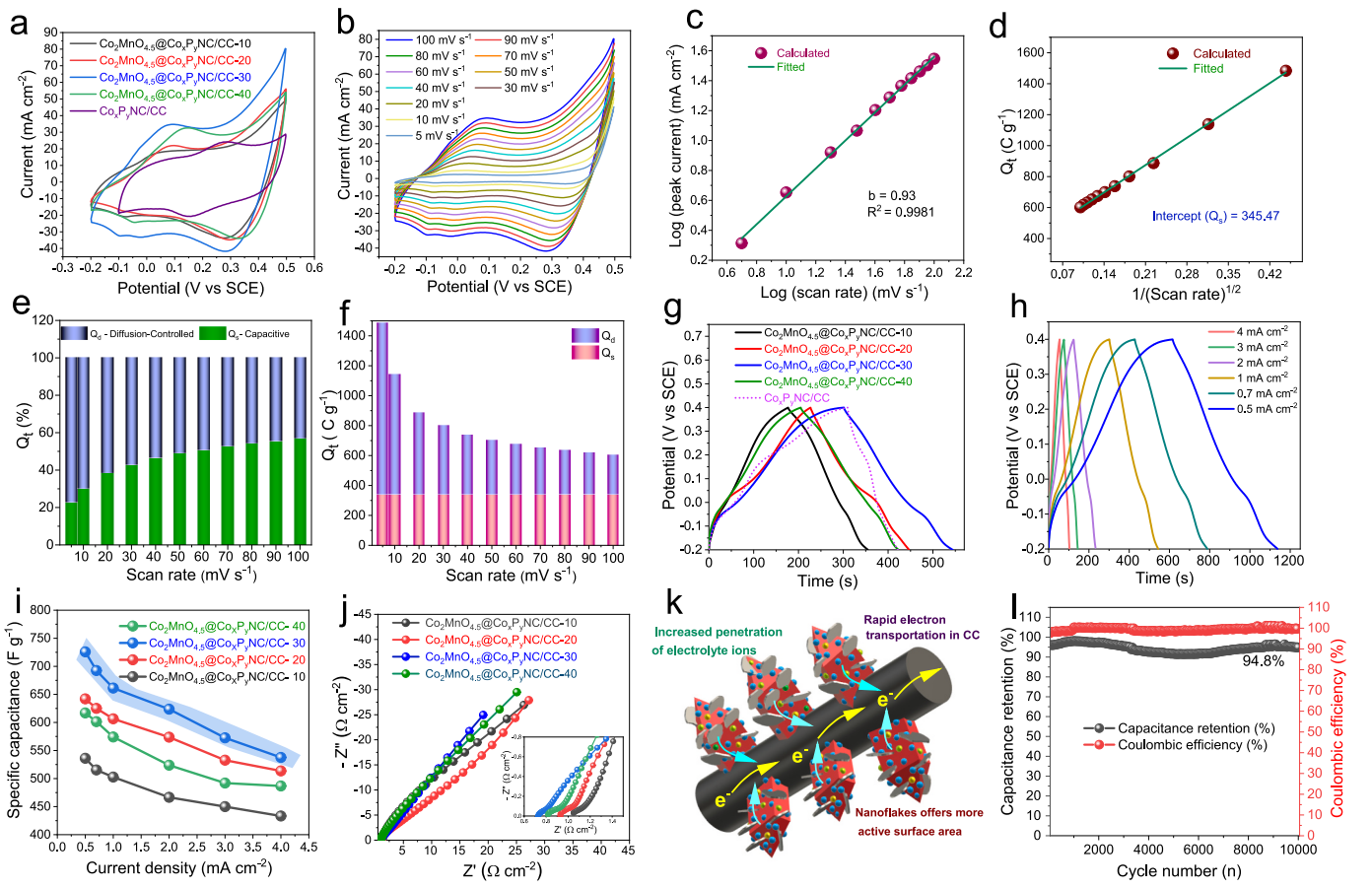

Fig. 4. (a) Comparative CV of the $Co_2MnO_{4.5}$@Co_xP_yNC/CC-10-40 and Co_xP_yNC/CC, (b) CV of $Co_2MnO_{4.5}$@Co_xP_yNC/CC-30, (c) Log of peak current *vs* log of scan rate plots, (d) Q_t *vs* 1/scan rate^{-1} plots, (e and f) Q_t (%) and Q_t *vs* scan rate plots with Q_s and Q_d, (g) Representative GCD curves of $Co_2MnO_{4.5}$@Co_xP_yNC/CC-10-40, (h) GCD curves of $Co_2MnO_{4.5}$@Co_xP_yNC/CC-30 at 0.5–4 mA cm^{-2}, (i) C_s *vs* current density plots, (j) Nyquist plots, (k) Schematic of electrode, and (l) C_s retention (%) along with Coulombic efficiency (%) against cycle plots of $Co_2MnO_{4.5}$@Co_xP_yNC/CC-30 electrode.

electrodes (Fig. 4j). The $Co_2MnO_{4.5}$@Co_xP_yNC/CC-30 electrode exhibited low solution resistance (R_s) and charge-transfer resistance (R_{ct}) of 0.71 and 0.9 Ω cm^{-2}, respectively. The equivalent-circuit fitting is good agreement with the experimental data, as shown by a low χ^2 value of 0.0034085 and a sum of squared residuals of 0.41243. Moreover, the W—P parameter exhibited a relative fitting error of only 1.395% for the estimated error of 0.0085734, while the fitted curves closely matched the experimental Nyquist and Bode plots, confirming the reliability of the proposed equivalent-circuit model. The optimized electrode exhibits excellent electrochemical parameters, resulting from the structural engineering of electrode, phosphidation, and core-shell structure and morphology obtained from the SILAR method (Fig. 4k). The $Co_2MnO_{4.5}$@Co_xP_yNC/CC-30 electrode exhibits a C_s retention of 94.8% after 10,000 GCD cycles, with a Coulombic efficiency ~99% (Fig. 4l). The SEM images of the electrode after stability test and corresponding elemental mapping with EDS spectra shows the preserved surface structure of electrode even after long term stability test (Fig. S5 and S6). Excellent conductivity, quick charge transfer, less volume expansion of electroactive materials are all accountable for the exceptional cycle stability [49].

2.3. DFT simulations

To investigate the enhanced capacity of the CoP@$MnCo_2O_4$ heterostructure compared with bare CoP as a material for SC, the density functional theory (DFT) was carried out. The adsorption strength of OH^- directly connected to storage capacitance of electrode material and thereby quickening the kinetics of the redox reaction [50–53]. Therefore, we compared the adsorption energies of CoP@$MnCo_2O_4$ and bare CoP to investigate the effect of the heterostructure with $MnCo_2O_4$ on the enhancement of C_s in the CoP (Figs. S7-S9). The side (up) and top (down) views of the optimized structures of the CoP (211) slab, $MnCo_2O_4$ (311) slab, and CoP@$MnCo_2O_4$ heterostructure is depicted in Fig. 5a. Our results in Fig. 5b specify adsorption energy of CoP@$MnCo_2O_4$ (−5.57 eV) is further negative as of bare CoP (−3.76 eV), indicating more adsorption of electrolyte ions on CoP@$MnCo_2O_4$ than bare CoP. It might be attributed to the more charge transfer to OH (0.77 e$^-$) from CoP@$MnCo_2O_4$ than bare CoP (0.68 e$^-$) (Fig. 5c). This strong OH adsorption energy highlights the CoP@$MnCo_2O_4$ as an electrode for SC.

2.4. Characterization of MWCNT/MXene/CC negative electrodes

MXene sheets suffer from the issues such as restacking, the sheets produce a 2D structure, significantly limits the electrolyte-ion penetration and leading to poor performance. These issues can be resolved by immersing nanowires of the MWCNT in the interlayer spacing of MXenes [26]. Herein, a binder-free MWCNT/MXene electrode was synthesized following previous works using a drop casting deposition method as described in the experimental section in Supporting Information [26,54]. The electrolyte ion's accessibility at each interface of sheets was improved by preventing the restacking of the 2D MXene sheets. Fig. 6a displays SEM pictures of the MWCNT/MXene/CC surface at magnifications of 200 kX. The homogenous and porous morphology, metallic conductivity, and 2D structure of electroactive MWCNT/MXene electrode material promote high energy storage capabilities. The TEM and HRTEM images of the MWCNT/MXene material are depicted in Fig. 6b

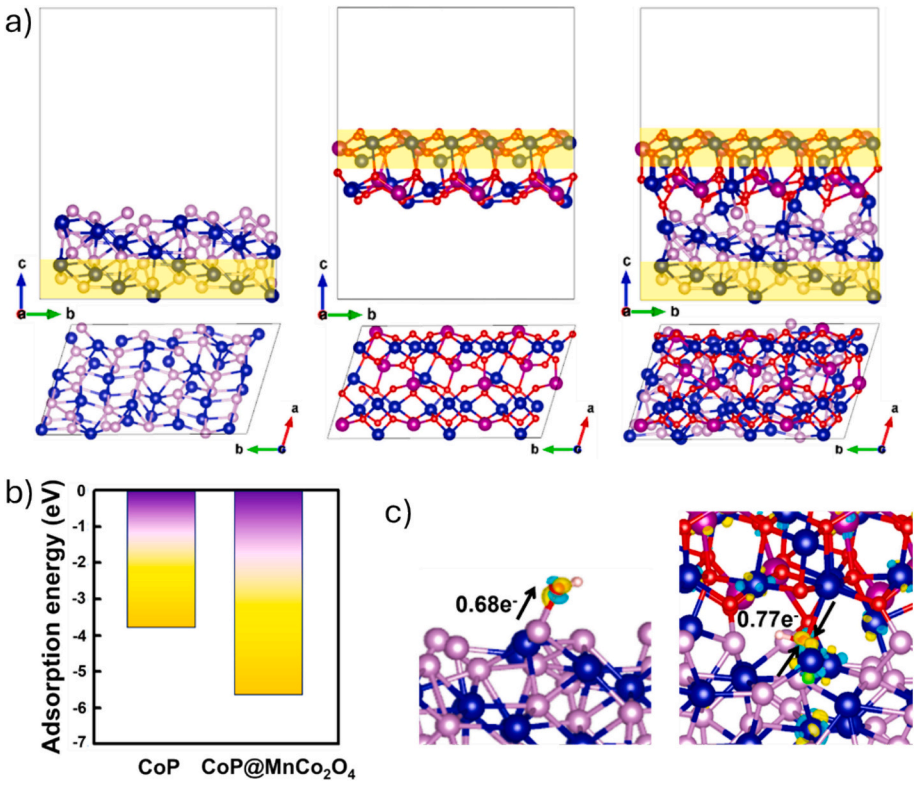

Fig. 5. a) Side (Up) and top (down) views of the optimized structures CoP (211) slab, $MnCo_2O_4$ (311) slab, and CoP@$MnCo_2O_4$ heterostructure. The atoms in the yellow region were fixed to describe the bulk region, b) Adsorption energy of OH on CoP and CoP@$MnCo_2O_4$, c) Charge transfer to OH from CoP and CoP@$MnCo_2O_4$. Yellow/blue isosurfaces represent electron accumulation/depletion, respectively. (For interpretation of the references to colour in this figure legend, the reader is referred to the web version of this article.)

and c. The MWCNT nanowires and 2D MXene sheets are clearly visualized in the TEM image. Furthermore, the atomic structure of the $Ti_3C_2T_X$ layers with Ti, C and functional groups arrangements are clearly seen in the HRTEM image.

The XRD pattern of MWCNT/MXene is shown in Fig. 6d. A distinct diffraction peaks appeared for the hkl planes of (002), (004), and (006) of the MXene, meanwhile the diffraction peak shifted to lower angle of 6.2° confirm the formation of MWCNT/MXene composite electrode [26,54–56]. The deconvoluted C1s spectra shown in Fig. 6e fitted to C-Ti-T_x, C-C/C=C, and O=C-O peaks. Significant π-π interactions and forces generated by sp^2 structure of MWCNT, resulting in the strong adherence to the layer of $Ti_3C_2T_X$ sheets [26,55,56]. Ti 2p peaks separated into Ti $2p_{3/2}$ as well as Ti $2p_{1/2}$ at 455 and 463 eV, respectively and the spectra is deconvoluted into Ti—C (455.0, 458.93 eV), Ti—O (457.60, 463.57 eV), and Ti-II (456.18, 461.32 eV), respectively (Fig. 6f) [26]. Fig. 6g shows the deconvoluted spectra of O 1 s (Ti-O-H, C-Ti-O, C-Ti-$(OH)_X$). The deconvoluted spectrum of F 1 s was divided into peaks for C-Ti-F_X (684.91 eV), TiO_{2-X}, and/or AlF_3 (886.63 eV) as depicted in Fig. 6h [19,26]. The elemental mapping of electrode surface was carried out to confirm the elements with appropriate percentage (Fig. 6i-o).

2.5. Electrochemical analysis of MWCNT/MXene based electrode

The CV of the MWCNT/MXene/CC electrode was tested at 5–100 mV s^{-1} within −0.1 to −1.0 V/SCE (Fig. 7a). The intercalation pseudocapacitive behavior confirmed with not appearance of redox peak in the CV curves for all scan rates [57]. The material maintains the rate of redox reaction continually, which indicates that CV has a rectangular shape without a redox peak. The charge storage in the electrode is made up of two components: the non-faradaic electrochemical double layers, and the slow ion diffusion regulated with faradaic intercalation reactions. The b-value of 0.96 suggests charge storage by surface control, and the R^2 value of 0.9943 supports the linearity and reliability of the fitting, as well as the fact that the current response follows the expected power-law relationship (Fig. 7b) [44,57]. The capacitive contribution of electrode through surface-controlled reactions Q_s is the intercept of the Q_t *vs* (1/scan rate) $^{1/2}$ plot (Fig. 7c). At 100 mV s^{-1}, the Q_s and Q_d are determined to be 96.28% and 3.71%, respectively and it's changed to 74.83% and 25.16% at 5 mV s^{-1} (Fig. 7d). Fig. 7e compares the charge distribution of Q_s and Q_d. The GCD measurements of the electrode were tested at 3–10 mA cm^{-2} (Fig. 7f). The C_s was determined to be 195 F g^{-1} for 3 mA cm^{-2} and it retained 175 F g^{-1} at 10 mA cm^{-2} (Fig. 7g). MWCNT/MXene negative electrode have low R_s and R_{ct} values (1.27 Ω cm^{-2} along with 1.51 Ω cm^{-2}, respectively), suggesting superior electrical conductivity (Fig. 7h). The C_s retention (%) besides the Coulombic efficiency (%) against cycle plots are depicted in Fig. 7i. The MWCNT/MXene/CC retained a C_s of 95.8% over 9500 cycles while maintaining a Coulombic efficiency of ~96% at 15 mA cm^{-2}.

2.6. Fabrication of quasi-solid-state device (QSSD)

The QSSD was fabricated with $Co_2MnO_{4.5}$@Co_xP_yNC/CC-30 and MWCNT/MXene positive and negative electrodes, and gel-type polyvinyl alcohol-potassium hydroxide (PVA-KOH) electrolyte (Fig. 8a). The CV curves of positive and negative electrodes are displayed in Fig. 8b within the voltage of −0.2 to 0.5 and − 0.1 to −1.0 V/SCE, respectively, at 50 mV s^{-1}. The CV predicts the maximum voltage window of the QSSD device and it is expected to be 1.5 V. To determine the accurate potential of QSSD, the CV are curves measured within 1.1 to 1.6 V (Fig. 8c). The sharp current response and comparative decrement in the integral area under the CV after 1.5 V, indicating the desired potential of QSSD is ~1.5 V. The GCD analysis predicts the accuracy of the working potential window by recording GCD curves at various potentials, indicating that the potential is suitable within the range of 1.4 to 1.5 V (Fig.

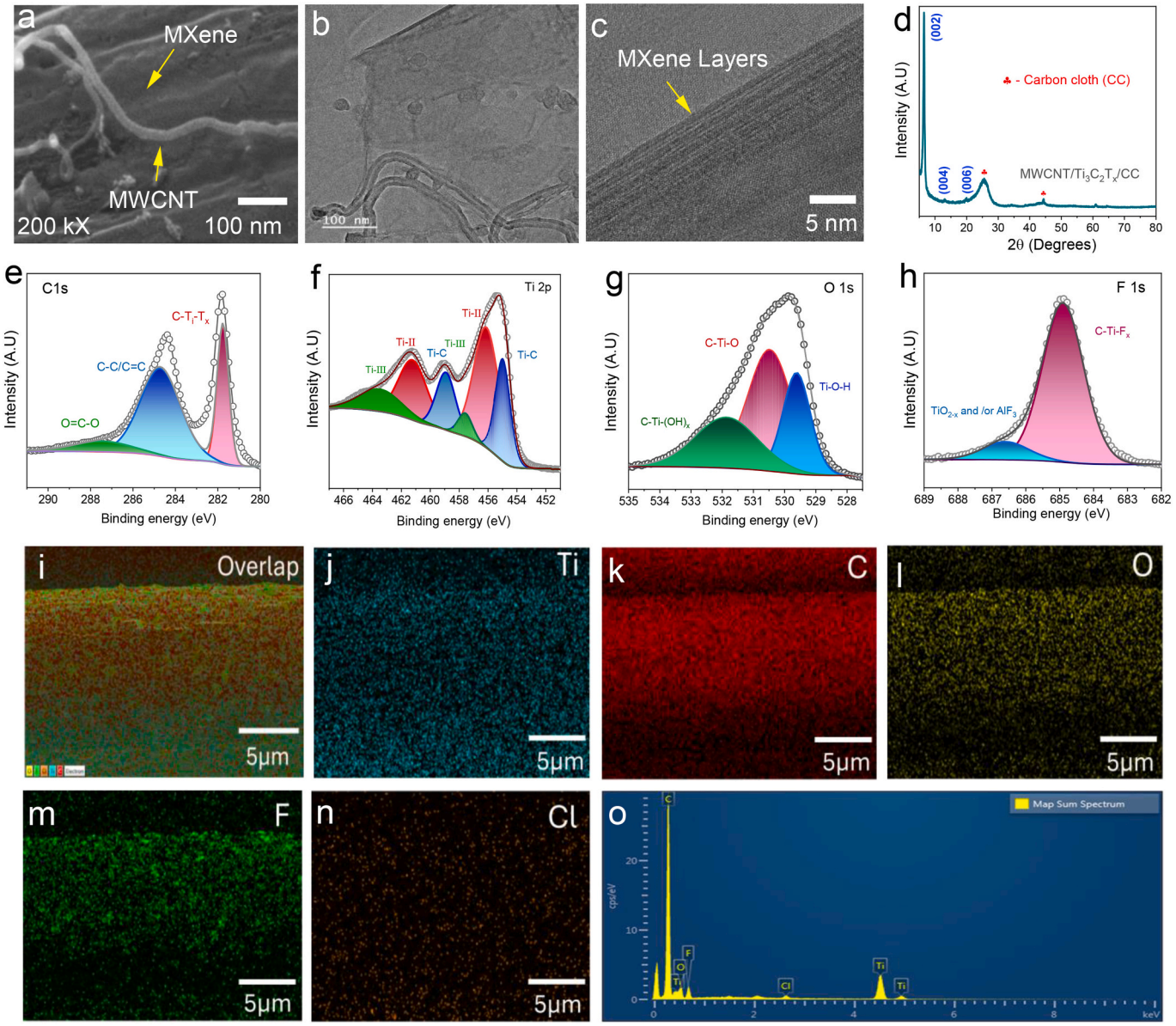

Fig. 6. (a-c) SEM and TEM images, (d) XRD pattern, Deconvoluted spectra of the (e) C1s, (f) Ti2p, (g) O1s, (h) F1s, and Elemental mapping with (i) overlap image, (j) Ti element, (k) C element, (l) O element, (m) F element, (n) Cl element and (o) EDS spectra.

S10). The CV curves of QSSD devices were measured at 10–100 mV s^{-1} as demonstrated in Fig. 8d. The CV curves exhibit nearly symmetric CV profiles, with redox peaks on anodic and cathodic sides. The peaks represent the alteration of the Co^{+2}/Co^{+3} and Mn^{+2}/Mn^{+3} states of the electrode material, resulting in more effective interfacial kinetics and quick ionic/electronic diffusion rates [46–48]. The GCD curves of QSSD were measured within the 0.25–2.5 A g^{-1} within 1.4 V (Fig. 8e). The nearly symmetric charge discharge segment at all current densities with extended times in the GCD curves indicates the excellent energy density with outstanding Coulombic efficiency and reversibility. The longer discharge time is observed at lower current owing to adequate time for electrolyte ion intercalation in the electrode material, resulting in a minimal internal resistance (IR) drop. The QSSD device has C_s of 183.9 F g^{-1} at 0.25 A g^{-1} (Fig. 8f). The calculated C_s of QSSD at 1 A g^{-1} is compared with $PMo10V_2$@ZIF67//AC (76.9 F g^{-1}) [10], Co/Mn-ZIF//AC (67.25 F g^{-1}) [58], SS/MP_3//$MgSO_4$//MP_3/SS (73 F g^{-1}) [59], RGO//RGO-CNF-$MnCO_3$ (27.7 F g^{-1}) [60], HNCS//CoP/C (59.3 F g^{-1}) [61], CN-30//NiCo-LDH and NBC-Fe_2O_3@Mn_2O_3 (96.6 F g^{-1}) [62], NiCoP/NF//N-rGO/NF (64.3 F g^{-1}) [63], graphene//Ni-CoP@C@CNT (64 F g^{-1}) [64], AC//Ni-P (50 F g^{-1}) [65], and AC//Ni-P@MnO_2 (62 F g^{-1}) [65] (Fig. 8g).

The calculated energy along with power density of the QSSD device were plotted in Fig. 8h. The highest energy density of 50.06 Wh kg^{-1} was observed at 175 W kg^{-1}. Furthermore, the uppermost power density of 1750 W kg^{-1} was obtained at 20.41 Wh kg^{-1}. The energy density values obtained in this work are better than the reported devices of Mn-CoP/NF//AC [66], MnO_2@MnO_2//MnO_2@MnO_2 [67], V_2O_5/PP_y//V_2O_5/PP_y [68], $FeCo_2O_4$@MnO_2//AC [69], and rGO/Ppy/PVA-H_2SO_4/WO_3 [70]. The Nyquist plot of before and after stability displayed a reduced resistance value (Fig. 8i). The capacitive behavior of is QSSD confirmed by the appearance of a semicircle at a high frequency region and the electrolyte ion penetration strength by straight line with an inclination ~45°. The lower values of R_s and R_{ct} are observed to be 2.22 Ω cm^{-2} and 0.927 Ω cm^{-2} for the before stability and 2.61 Ω cm^{-2}, 1.22 Ω cm^{-2} for the after stability of QSSD device demonstrate its greater performance with less resistance. After 10,000 GCD cycles, the QSSD device maintained 96.5% C_s retention and ~ 99% Coulombic efficiency, showing superior reversibility and durability (Fig. 8j). The 3.5% decline

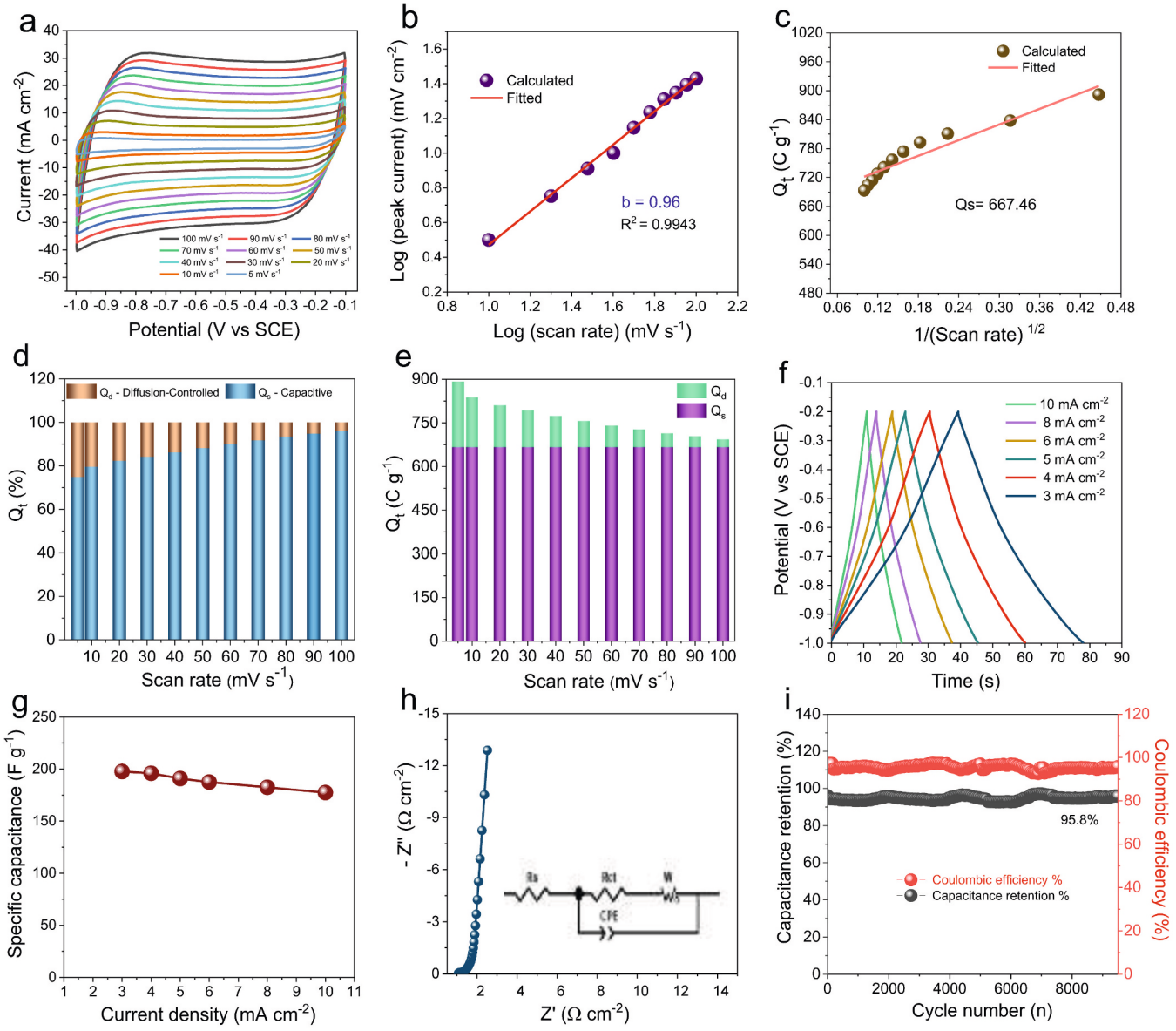

Fig. 7. (a) CV of MWCNT/MXene/CC, (b) Log of current density with log of scan rates plot, (c) Q_t *vs* 1/(scan rate)$^{1/2}$ plots, (d) The percentage wise distribution of Q_t with Q_s and Q_d, (e) Q_t *vs* scan rate plots, (f) GCD at current densities of the 3–10 mA cm^{-2}, (g) The C_s with current density plots, (h) Nyquist plots with fitted equivalent circuit, and (i) C_s retention (%) along with Coulombic efficiency (%) *versus* cycle number plots.

in C_s might be due to structural degradation, active material loss from the CC, lower ionic conductivity, or slower electron transport. The CV and GCD measurements of the QSSD were performed within slightly different potential windows based on the electrochemical stability of the device. The CV measurements were conducted from 0 to 1.5 V, whereas the GCD measurements and cycling stability test were performed from 0 to 1.4 V. The slightly narrower GCD window was deliberately selected to minimize polarization, possible side reactions, electrolyte decomposition, and electrode/electrolyte interfacial degradation during prolonged GCD cycling [45]. This approach ensures stable and reliable GCD profiles and improves the long-term cycling stability of the QSSD. The overall electrochemical performance of the QSSD device compared with previously reported works (**Table S1**). [1,10,59–65,69,71–78] The real-world applicability of the QSSD device were verified by linking light-emitting diodes (LEDs) to the series connected two QSSDs (Fig. 8k). The two series connected QSSDs were charged up to 30 s and connected to LEDs. The LEDs were glowing for a minute with intensity, demonstrating the QSSD has great power and energy density.

3. Conclusions

In conclusion, we report a rationally engineered core-shell $Co_2MnO_{4.5}$@Co_xP_yNC/CC electrode, in which Co—Mn oxide nanoflakes are uniformly anchored onto a MOF-derived nitrogen-doped porous carbon micro-petal scaffold. The synergistic integration of the conductive Co_xP_yNC framework with electroactive $Co_2MnO_{4.5}$ nanostructures provides abundant accessible active sites, accelerated ion/electron transport kinetics, and enhanced structural robustness. Owing to its high surface area, low internal resistance, and mechanically stable core-shell architecture, the electrode delivers an outstanding C_s of 725.8 F g^{-1} at 0.5 mA cm^{-2} together with remarkable cycling durability, retaining 94.8% of its C_s after 10,000 GCD cycles. Density functional theory calculations further corroborate the experimental observations by revealing favorable OH^- adsorption energetics on the core-shell surface, highlighting the origin of the enhanced charge-storage behavior. Moreover, the assembled quasi-solid-state supercapacitor based on $Co_2MnO_{4.5}$@Co_xP_yNC/CC and MWCNT/MXene electrodes achieves a high energy

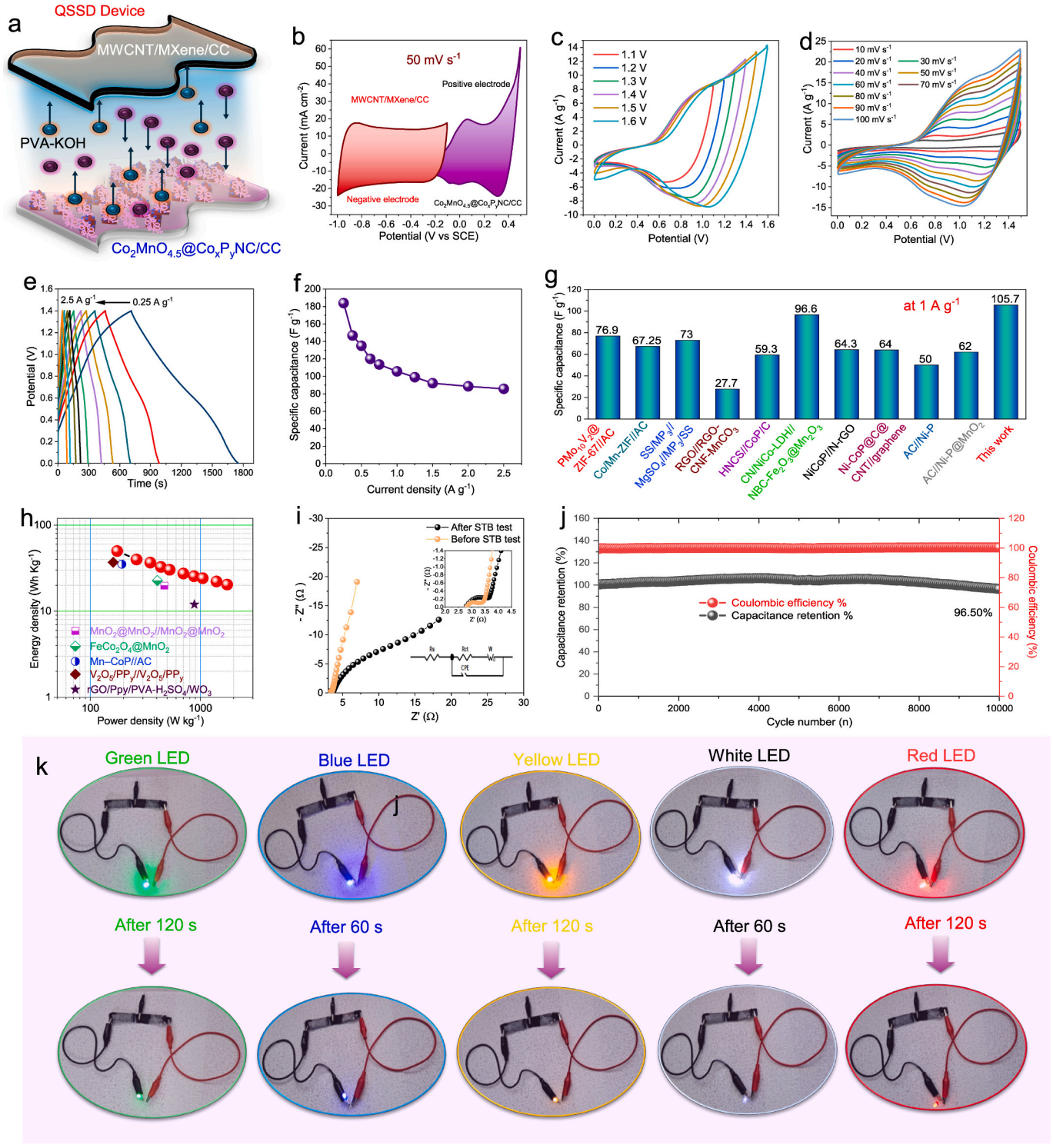

Fig. 8. (a) Schematic of QSSD, (b) CV at 50 mV s^{-1}, (c) The windows selection CV curves at 1.1–1.6 V, (d) CV curves of QSSD device, (e) GCD curves of QSSD at 0.25–2.5 A g^{-1}, (f) The C_s *vs* current density plots, (g) Comparison of C_s of QSSD with previous reports, (h) Ragone plots, (i) Nyquist plot (inside shows fitted circuit and magnified Nyquist plot), and (j) Stability plots, and (k) Demonstration of QSSD device by glowing LEDs.

density of 50.06 Wh kg^{-1} with excellent long-term stability of 96.5% over 10,000 cycles. These findings demonstrate that MOF-derived hierarchical core-shell nanoarchitectures represent a highly promising strategy for developing next-generation high-performance energy-storage systems.

CRediT authorship contribution statement

Arti A. Jadhav: Writing – review & editing, Writing – original draft, Methodology, Investigation, Formal analysis, Data curation, Conceptualization. **Amar M. Patil:** Writing – review & editing, Writing – original draft, Visualization, Validation, Supervision, Methodology, Investigation, Formal analysis, Data curation, Conceptualization. **Seongyeon**

Hwang: Writing – review & editing, Writing – original draft, Software. **Jongwoo Hong:** Methodology, Formal analysis, Data curation. **Ganesh D. Jadhav:** Writing – review & editing, Writing – original draft. **Suprimkumar D. Dhas:** Writing – review & editing, Writing – original draft. **Tayebeh Ameri:** Writing – review & editing, Visualization, Validation, Supervision. **Kyeounghak Kim:** Writing – review & editing, Writing – original draft, Visualization, Supervision, Software. **Seong Chan Jun:** Writing – review & editing, Writing – original draft, Visualization, Validation, Supervision, Investigation, Funding acquisition. **Umakant M. Patil:** Writing – review & editing, Writing – original draft, Visualization, Validation, Supervision, Methodology, Investigation, Funding acquisition, Formal analysis, Conceptualization.

Declaration of competing interest

The authors declare that they have no known competing financial interests or personal relationships that could have appeared to influence the work reported in this paper.

Acknowledgements

This research was supported by multiple funding sources: the D. Y. Patil Education Society, Kasaba Bawada, Kolhapur, under the internal university research project (Sanction No. DYPES/DU/R&D/2022/2353); the National Research Foundation of Korea (NRF), funded by the Korean government (MSIT) (RS-2024-00339770); and the Korea Environment Industry & Technology Institute (KEITI) through the Technology Development Project for Biological Hazards Management in Indoor Air Program, sponsored by the Ministry of Environment (MOE) (ARQ202101038001).

Appendix A. Supplementary data

Supplementary data to this article can be found online at https://doi.org/10.1016/j.est.2026.124894.

Data availability

Data will be made available on request.

References

[1] C. Shi, K.A. Owusu, X. Xu, T. Zhu, G. Zhang, W. Yang, L. Mai, Small 15 (48) (2019) e1902348.
[2] G. Terren-Serrano, R. Deshmukh, M. Martinez-Ramon, Nat. Commun. 17 (2026) 3307.
[3] J.A. Goudar, T.S. N., S. Chapi, M.M. V., M.R. Saeb, M. Salami-Kalajahi, Adv. Energy Sustainability Res. 6 (2) (2024) 2400271.
[4] Y. Li, J. Zhang, Q. Chen, X. Xia, M. Chen, Adv. Mater. 33 (27) (2021) e2100855.
[5] Y. Shao, Y. Zhao, H. Li, C. Xu, ACS Appl. Mater. Interfaces 8 (51) (2016) 35368.
[6] X. Li, A.M. Elshahawy, C. Guan, J. Wang, Small 13 (39) (2017) 1701530.
[7] Q. Zong, C. Liu, H. Yang, Q. Zhang, G. Cao, Nano Today 38 (2021) 101201.
[8] F. Zhan, H. Wang, Q. He, W. Xu, J. Chen, X. Ren, H. Wang, S. Liu, M. Han, Y. Yamauchi, L. Chen, Chem. Sci. 13 (41) (2022) 11981.
[9] R. Robson, Chem. Rec. 24 (5) (2024) e202400038.
[10] A.M. Mohamed, M. Ramadan, N. Ahmed, A.O. Abo ElNaga, H.H. Alalawy, T. Zaki, S.A. Shaban, H.B. Hassan, N.K. Allam, J. Energy Storage 28 (2020) 101292.
[11] A.M. Mohamed, A.O. Abo El Naga, T. Zaki, H.B. Hassan, N.K. Allam, ACS Appl. Energy Mater. 3 (8) (2020) 8064.
[12] L. Xu, Y. Xi, W. Li, Z. Hua, J. Peng, J. Hu, J.-J. Zhou, P. Zhang, J. Wang, W. Wang, H. Ding, W. Wang, W. Ji, Y. Yang, X. Xu, L. Chen, X. Li, Nano Energy 91 (2022) 106630.
[13] Y. Lin, K. Sun, S. Liu, X. Chen, Y. Cheng, W.C. Cheong, Z. Chen, L. Zheng, J. Zhang, X. Li, Y. Pan, C. Chen, Adv. Energy Mater. 9 (36) (2019) 1901213.
[14] P. Arunkumar, S. Gayathri, D. Saha, J. Hun Han, J. Colloid Interface Sci. 635 (2023) 562.
[15] S. Gayathri, P. Arunkumar, D. Saha, J.H. Han, J. Colloid Interface Sci. 588 (2021) 557.
[16] F. Li, G. Li, H. Chen, J.Q. Jia, F. Dong, Y.B. Hu, Z.G. Shang, Y.X. Zhang, J. Power Sources 296 (2015) 86.
[17] V.G. Parale, T. Kim, A.M. Patil, V.D. Phadtare, H. Choi, R.P. Dhavale, Y. Kim, S. C. Jun, H.H. Park, Int. J. Energy Res. 46 (4) (2021) 5250.
[18] A.M. Patil, S. Moon, Y. Seo, S.B. Roy, A.A. Jadhav, D.P. Dubal, K. Kang, S.C. Jun, Small 19 (5) (2023) e2205491.
[19] A.M. Patil, S. Moon, S.B. Roy, J. Ha, N.R. Chodankar, D.P. Dubal, A.A. Jadhav, G. Guan, K. Kang, S.C. Jun, Small 19 (37) (2023) e2301153.
[20] W.C. Huo, X.L. Liu, Y.S. Yuan, N. Li, T. Lan, X.Y. Liu, Y.X. Zhang, Front. Chem. 6 (2018) 661.
[21] H.C. Chen, S. Jiang, B. Xu, C. Huang, Y. Hu, Y. Qin, M. He, H. Cao, J. Mater. Chem. A 7 (11) (2019) 6241.
[22] H. Chen, M. Zhou, T. Wang, F. Li, Y.X. Zhang, J. Mater. Chem. A 4 (28) (2016) 10786.
[23] L. Bao, J. Zang, X. Li, Nano Lett. 11 (3) (2011) 1215.
[24] S. Liu, D. Gao, J. Li, K.S. Hui, Y. Yin, K.N. Hui, S. Chan Jun, J. Mater. Chem. A 7 (46) (2019) 26618.
[25] A.M. Patil, S. Moon, A.A. Jadhav, J. Hong, K. Kang, S.C. Jun, Adv. Funct. Mater. 33 (46) (2023) 2305264.
[26] A.M. Patil, N.R. Chodankar, E. Jung, S. Roy, D.P. Dubal, G. Guan, Y.-K. Han, S. C. Jun, J. Mater. Chem. A 9 (46) (2021) 26135.
[27] A.M. Patil, A.A. Jadhav, N.R. Chodankar, A.T. Avatare, J. Hong, S.D. Dhas, U. M. Patil, S.C. Jun, Coord. Chem. Rev. 517 (2024) 216020.
[28] M. Naguib, M. Kurtoglu, V. Presser, J. Lu, J. Niu, M. Heon, L. Hultman, Y. Gogotsi, M.W. Barsoum, Adv. Mater. 23 (37) (2011) 4248.
[29] Y. Liu, C. Wang, H. Sun, L. Duan, Z. Yang, X. Wang, J. Liu, J. Colloid Interface Sci. 682 (2025) 1051.
[30] Z. Sun, B. Bai, J. Shui, X. Xie, P. Du, J. Energy Storage 100 (2024) 113637.
[31] J. Bhagwan, S.K. Hussain, B.N. Vamsi Krishna, J.S. Yu, J. Ind. Eng. Chem. 94 (2021) 292.
[32] K. Hua, X. Li, Z. Rui, X. Duan, Y. Wu, D. Yang, J. Li, J. Liu, ACS Catal. 14 (5) (2024) 3712.
[33] S.V. Mohite, R. Xing, B. Li, S.S. Latthe, Y. Zhao, X. Li, L. Mao, S. Liu, Inorg. Chem. 59 (3) (2020) 1996.
[34] C.-W. Tang, C.-B. Wang, S.-H. Chien, Thermochim. Acta 473 (1–2) (2008) 68.
[35] C.M. Julien, M. Massot, C. Poinsignon, Spectrochim. Acta A Mol. Biomol. Spectrosc. 60 (3) (2004) 689.
[36] W. Li, J. Chen, F. Xie, H. Zhu, L. Sun, K. Wang, J. Energy Storage 104 (2024) 114492.
[37] S. Liu, K. San Hui, K.N. Hui, J.M. Yun, K.H. Kim, J. Mater. Chem. A 4 (21) (2016) 8061.
[38] X. Fu, Z. Zhang, Y. Zheng, J. Lu, S. Cheng, J. Su, H. Wei, Y. Gao, J. Colloid Interface Sci. 653 (Pt B) (2024) 1272.
[39] N. Karuppusamy, V. Mariyappan, S.M. Chen, M.D. Thangamuthu, R.-H. Li, Surf. Interfaces 37 (2023) 102681.
[40] C. Yuan, J. Li, L. Hou, X. Zhang, L. Shen, X.W. Lou, Adv. Funct. Mater. 22 (21) (2012) 4592.
[41] V. Sannasi, K. Subbian, Ceram. Int. 46 (10) (2020) 15510.
[42] A.M. Patil, X. An, S. Li, X. Yue, X. Du, A. Yoshida, X. Hao, A. Abudula, G. Guan, Chem. Eng. J. 403 (2021) 126411.
[43] M.Z. Iqbal, U. Abbasi, M. Alzaid, J. Energy Storage 50 (2022) 104632.
[44] J.P. John Wang, James Lim, Bruce Dunn, J. Phys. Chem. C 111 (2007) 14925.
[45] A.M. Patil, H.M. You, A.A. Jadhav, J. Hong, S.K. Das, S.D. Dhas, T.J. Lim, E. Lee, K. Y. Chung, K. Kim, S.C. Jun, Adv. Energy Mater. 15 (3) (2024) 2403322.
[46] S. Liu, Y. Yin, D. Ni, K.S. Hui, M. Ma, S. Park, K.N. Hui, C.-Y. Ouyang, S.C. Jun, Energy Storage Mater. 22 (2019) 384.
[47] J. Wu, L. Yan, H. Huang, Y. Liang, C. Li, F. Yuan, X. Liang, W. Zhou, J. Guo, ACS Appl. Nano Mater. 6 (20) (2023) 18837.
[48] M. Jing, H. Hou, Y. Yang, Y. Zhu, Z. Wu, X. Ji, Electrochim. Acta 165 (2015) 198.
[49] S. He, F. Guo, Q. Yang, H. Mi, J. Li, N. Yang, J. Qiu, Small 17 (21) (2021) e2100353.
[50] R. Tang, H. Li, Y. Zhang, Y. Zhao, Y. Wu, J. Energy Storage 110 (2025) 115237.
[51] S. Wei, C. Wan, L. Zhang, X. Liu, W. Tian, J. Su, W. Cheng, Y. Wu, Chem. Eng. J. 429 (2022) 132242.
[52] B. Shen, X. Liao, X. Hu, H.-T. Ren, J.-H. Lin, C.-W. Lou, T.-T. Li, J. Mater. Chem. A 11 (31) (2023) 16823.
[53] X. Chen, N. Xin, Y. Li, C. Sun, L. Li, Y. Ying, W. Shi, Y. Liu, J. Mater. Sci. Technol. 127 (2022) 236.
[54] A.A. Jadhav, A.M. Patil, G.D. Jadhav, S. Hwang, M. Islam, J. Joo, J. Hong, K. Kim, S.C. Jun, U.M. Patil, J. Energy Storage 162 (2026) 122099.
[55] M.W. Hakim, I. Ali, S. Fatima, H. Li, S.H.M. Jafri, S. Rizwan, ACS Omega 9 (8) (2024) 8763.
[56] N.K. Gautam, A. Alshoaibi, S. Lavania, G. Dhiman, M. Nasit, S. Dalela, P.A. Alvi, R. K. Brajpuriya, A. Sharma, S. Kumar, Diam. Relat. Mater. 160 (2025) 113046.
[57] Maria R. Lukatskaya, Olha Mashtalir, Chang E. Ren, Yohan Dall'Agnese, Patrick Rozier, Pierre Louis Taberna, Michael Naguib, Patrice Simon, Michel W. Barsoum, Y. Gogotsi, Science 341 (2013) 1502.
[58] W. Yang, X. Shi, Y. Li, H. Pang, J. Energy Storage 26 (2019) 101018.
[59] K. Belekar, S. Patil, S. Kumbhar, S. Bhosale, G. Jadhav, C. Lokhande, U. Patil, Solid State Commun. 401 (2025) 115916.
[60] B. Amutha, M. Sathish, J. Solid State Electrochem. 19 (8) (2015) 2311.
[61] X. Zhang, S. Hou, Z. Ding, G. Zhu, H. Tang, Y. Hou, T. Lu, L. Pan, J. Alloys Compd. 822 (2020) 153578.
[62] Y. Wang, S. Wei, F. Ren, X. Zhu, X. Lu, Z. Li, C. Wang, H. Li, Y. Su, Q. Su, J. Liang, J. Energy Storage 103 (2024) 114277.
[63] P. Li, Y. Han, F. Yan, L. Yan, H. Huang, W. Zhou, J. Energy Storage 38 (2021) 102503.
[64] J. Gu, L. Sun, Y. Zhang, Q. Zhang, X. Li, H. Si, Y. Shi, C. Sun, Y. Gong, Y. Zhang, Chem. Eng. J. 385 (2020) 123454.

[65] X. Li, R. Ding, W. Shi, Q. Xu, L. Wang, H. Jiang, Z. Yang, E. Liu, Mater. Lett. 187 (2017) 144.
[66] G. Zhu, L. Yang, W. Wang, M. Ma, J. Zhang, H. Wen, D. Zheng, Y. Yao, Chem. Commun. (Camb.) 54 (66) (2018) 9234.
[67] Y.M. Chen, B.Z. Yu, Y.Q. Miao, F. Gao, G.Y. Jing, H.M. Fan, Nanoscale 10 (29) (2018) 14352.
[68] Y. Liang, Z. Wei, X. Zhang, R. Wang, Energy Sustain Energy Environ. 18 (2022) 101.
[69] F. Zhu, Y. Liu, M. Yan, W. Shi, J. Colloid Interface Sci. 512 (2018) 419.
[70] D.C. Pawar, D.B. Malavekar, J.H. Kim, C.D. Lokhande, Electrochim. Acta 514 (2025) 145671.
[71] Y. Shang, T. Xie, Y. Gai, L. Su, L. Gong, H. Lv, F. Dong, Electrochim. Acta 253 (2017) 281.
[72] N.S. Neeraj, B. Mordina, A.K. Srivastava, K. Mukhopadhyay, N.E. Prasad, Appl. Surf. Sci. 473 (2019) 807.
[73] L. Yue, S. Zhang, H. Zhao, Y. Feng, M. Wang, L. An, X. Zhang, J. Mi, Solid State Ionics 329 (2019) 15.
[74] J. Bhagwan, G. Nagaraju, B. Ramulu, S.C. Sekhar, J.S. Yu, Electrochim. Acta 299 (2019) 509.
[75] L. Xie, Y. Liu, H. Bai, C. Li, B. Mao, L. Sun, W. Shi, J. Colloid Interface Sci. 531 (2018) 64.
[76] X. Li, R. Ding, L. Yi, W. Shi, Q. Xu, E. Liu, Electrochim. Acta 222 (2016) 1169.
[77] J. Acharya, B.G.S. Raj, T.H. Ko, M.-S. Khil, H.-Y. Kim, B.-S. Kim, Int. J. Hydrog. Energy 45 (4) (2020) 3073.
[78] H. Gao, J. Xiang, Y. Cao, Appl. Surf. Sci. 413 (2017) 351.